Materials Characterization 196 (2023) 112639

Contents lists available at ScienceDirect

Materials Characterization

journal homepage: www.elsevier.com/locate/matchar

Review

Heat treatment of melt-grown alumina ceramics with trace glass fabricated by laser directed energy deposition

Dake Zhao [a,b], Dongjiang Wu [a], Fangyong Niu [a,*], Yunfei Huang [a], Guangyi Ma [a], Cong Zhou [c], Bi Zhang [c], Guanhui Ren [d,e]

[a] Key Laboratory for Precision and Non-traditional Machining Technology of Ministry of Education, Dalian University of Technology, Dalian 116000, China
[b] Institute of Intelligent Manufacturing, Guangdong Academy of Sciences, Guangzhou 510070, China
[c] Department of Mechanical and Energy Engineering, Southern University of Science and Technology, Shenzhen 518055, China
[d] Research and Development Department, Shenzhen Xinjinquan Precision Techonology Co., Ltd., Shenzhen 518055, China
[e] School of Mechanical Engineering, Shandong University, Jinan 250061, China

ARTICLE INFO

Keywords:
Additive manufacturing
Alumina
Mullite formation
Cracking-healing
Strength recovery

ABSTRACT

Laser directed energy deposition (LDED) is attractive for one-step additive manufacturing of melt-grown alumina-based ceramics for hot-end components. However, significant improvement of mechanical properties for this material remains a challenge. Here, the macro features, microstructure, and mechanical properties in response to heat treatment temperature are investigated, especially mullite formation, crack-healing, and strength recovery. The results showed that the material has good thermal stability with mass loss $\leq$0.3% at high temperatures. The dissolution of alumina into the glass and the formation of mullite near the alumina-glass interface during heat treatment are responsible for the decrease in alumina grain size. With the increase of heat treatment temperature, the strength first increased and then decreased, with a maximum increase to 504.38 MPa. The fracture toughness gradually increased to a maximum of 3.54 MPa·m$^{1/2}$. Defect repair (e.g., crack-healing) and residual stress relaxation are responsible for significantly increased sample strength.

1. Introduction

In order to improve the thermal efficiency of aero engines, advanced ceramics are being developed as high-temperature structural materials to replace superalloy used for hot-end components. Because superalloys currently used have difficulty meeting the demand for higher temperatures (e.g., > 1700 °C). Early research on advanced ceramics focused on C or SiC and their composites because of their outstanding heat resistance and high-temperature strength. However, these materials are susceptible to chemical reactions in aqueous oxygen environments, leading to degradation of mechanical properties and, in severe cases, catastrophic damage to the entire component. In addition, complex processes and long production cycles (e.g., repeated re-infiltration or pyrolysis) are also issues to consider when preparing C or SiC and their composites. In contrast, oxide ceramics have received increasing attention due to their excellent thermal and natural chemical stability. They have been utilized in hot end components such as combustors, exhaust nozzles, and blades [1–6].

Melt-grown alumina-based composites are considered potential high-temperature structural materials for manufacturing hot-end components due to their excellent properties (high melting point and low density), outstanding oxidation resistance, and good thermochemical stability [7,8]. Laser directed energy deposition (LDED), one of additive manufacturing methods [9,10], provides a fast and efficient method for preparing high-quality melt-grown ceramics [11–13]. However, microcracks and coarse grains limit the mechanical properties of this material [14,15]. For this reason, researchers have conducted much research using methods such as the addition of a second phase and external field assistance [16,17]. Recently, we have enhanced the mechanical strength of melt-grown alumina ceramics by adding a small amount of silica [18]. The flexural strength, fracture toughness, and microhardness were 310.1 MPa, 3.03 MPa·m$^{1/2}$, and 18.19 GPa, respectively. However, these properties need improvement considering the extremely harsh operating environment of hot-end components.

As a post-treatment method for material fabrication, heat treatment is widely used to manufacture ceramics. First, heat treatment can be applied to adjust ceramics properties, including alumina [19], Al_2O_3/SiO_2 [20], and SiC-based [21,22]. Second, heat treatment removes

* Corresponding author.
E-mail address: niufangyong@dlut.edu.cn (F. Niu).

https://doi.org/10.1016/j.matchar.2022.112639
Received 16 November 2022; Received in revised form 22 December 2022; Accepted 28 December 2022
Available online 30 December 2022

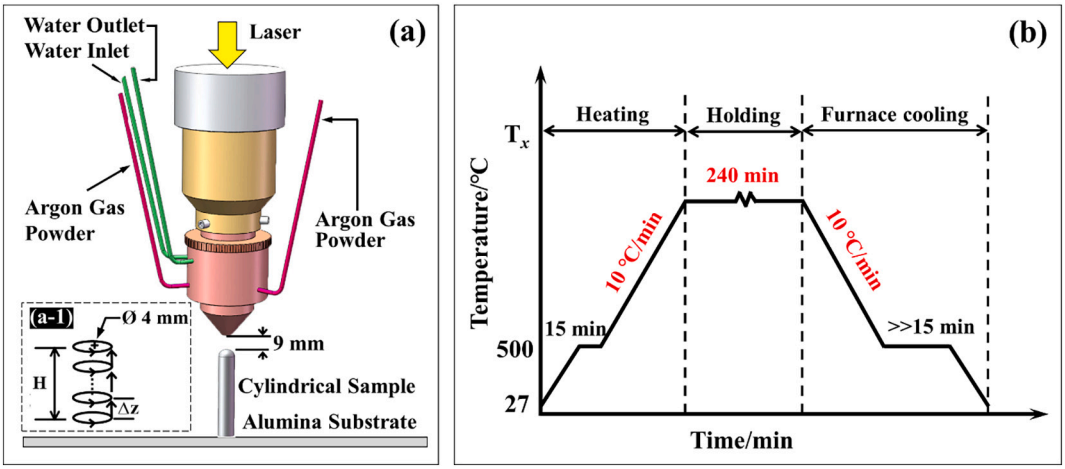

Fig. 1. (a) Schematic diagram of cylindrical samples prepared by LDED; (b) Heat treatment process.

organic binder or crystallizes inorganic binder for additive manufacturing ceramics to improve density and property. For example, Shahzad et al. [23] obtained alumina components with a density of 88% by suspended permeable indirect selective laser sintering (SLS) after hot isostatic sintering, with a flexural strength of 148 MPa. Heinrich et al. [24] used LSD-laser technology, a combination of layered slurry deposition (LSD) and laser sintering technology, to prepare alumina components with the compactness of 86%, increased to ~96% after heat treatment at 1600 °C. Gailevičius et al. [25] fabricated ZrO_2/SiO_2-rich ceramic materials with a resolution of about 100 nm using 3D direct laser writing. After heat treatment above 1200 °C, SiO_2 crystallized. The crystallized ZrO_2/SiO_2-rich ceramic materials were considered adaptable to harsh physical and chemical environments. The influence of heat treatment on melt-grown ceramics prepared by LDED has been less reported. Balla et al. [14], a pioneer in this field, first reported on heat treatment to improve properties (e.g., compressive strength and microhardness) of melt-grown alumina ceramics. However, the influence of heat treatment on microstructure and properties needs further investigation. Fan et al. [26] suggested that the color of yttria-stabilized zirconia (YSZ) ceramics recovered from dark brown to the same state as the original powder after heat treatment. Liu et al. [8] concluded that microstructure heterogeneity of melt-grown $Al_2O_3/GdAlO_3/ZrO_2$ ternary eutectic ceramics could be eliminated after heat treatment. Nevertheless, coarsened microstructure led to severe deterioration of mechanical properties and a lack of strength data [27]. For the goal of preparing high-performance melt-grown oxide ceramics by LDED, detailed insight into the relationship between the heat treatment process, microstructure, and mechanical properties is essential for the selection of a suitable heat-treatment process.

This work chose melt-grown alumina ceramics with trace glass prepared by LDED technology for the study. Heat treatment experiments with different holding temperatures were carried out in an air environment. The influence of temperature on macro features, microstructure, and mechanical properties was systematically investigated, focusing on phase composition, formation mechanism, and property recovery and enhancement. Based on the present work, significant strength enhancement of melt-grown oxide ceramics was achieved. The results of this work can provide a reference for the acceptance of melt-grown oxide ceramics prepared by LDED technology as a potential material for hot-end components.

2. Experiments and methods

2.1. As-received

The initial sample used in this work was melt-grown alumina ceramics with trace glass prepared by LDED technology with about 3 vol % of glass. The detailed preparation procedure referred to the previous report [18], and Fig. 1(a) shows a schematic diagram of the preparation of cylindrical samples by LDED technology. The cuboids were not prepared directly to evaluate the flexural strength because shaping accuracy is limited, and shaped samples require subsequent processing. The process parameters used to prepare the cylindrical samples were: laser power of 300 W, scanning speed of 250 mm/min, layer increment of 0.4 mm, and powder feeding rate of 2.51 g/min.

2.2. Heat treatment process

Cylindrical samples were sequentially ground into cuboids with 400#, 800#, 1500#, 2000#, and 3000# diamond discs. Then sample surface was polished to a mirror with a 2.5 μm diamond polishing paste. All subsequent characterization and testing were performed based on these cuboids. The heat treatment of the cuboid sample was carried out in a Muffle furnace with an air environment, and detailed heating and cooling routes are shown in Fig. 1(b). The heating rate was 10 °C/min, and the samples were cooled with the furnace. The heat treatment temperatures were 1000 °C, 1200 °C, 1400 °C, and 1600 °C, respectively. The holding time was 4 h. The formulation of the heat treatment process referred to Schmücker's research [28].

2.3. Characterization and detection

The oxygen elements in the samples before and after heat treatment were analyzed using the X-ray photoelectron spectroscopy (XPS) technique. The binding energy was corrected by C 1 s (284.6 eV). The thermogravimetry and heat flow changes as temperature increased from 50 °C to 1550 °C at 10 °C/min in an air environment were investigated using differential scanning calorimetry (DSC, TGA/SDTA851e, Mettler Company, Switzerland). The aim was to investigate thermal stability and possible phase transition at high temperatures. Infrared absorption spectra of samples in the range of 400–4000 cm^{-1} were measured using a Fourier transform infrared spectrometer (VERTEX70, Bruker Optics, Germany). >5 scans were collected for each sample. First, the cuboid samples were ground to a micron-sized powder using a mortar and pestle. Then, powder and dried KBr were mixed in a ratio of 1:100 and ground thoroughly to make the mixture homogeneous. The whole process was carried out in a dry environment. Finally, the mixed powder was pressed into almost transparent slices and then measured by projection infrared spectroscopy. The phase composition was analyzed by an x-ray diffractometer (XRD-6000, SHIMADZU, Japan) at an operating voltage and current of 40 kV and 30 mA, respectively. The microstructure was observed using a scanning electron microscope (Supra 55,

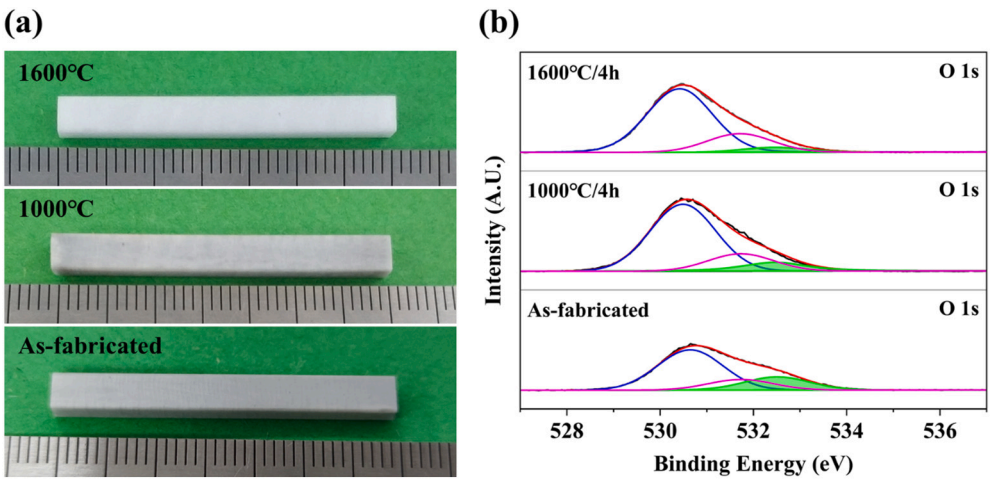

Fig. 2. Influence of heat treatment temperature on macro features of samples: (a) samples with and without heat treatment; (b) XPS curves of O 1 s.

Table 1
Comparison of O1s in samples with and without heat treatment.

Samples	BE/eV	Area/%	Origin of bonding
	530.64	63.29	Al_2O_3
As-prepared	531.73	13.16	Aluminosilicate
	532.51	23.54	Vacancy
	530.49	69.91	Al_2O_3
1000 °C	531.72	18.13	Aluminosilicate
	532.46	11.96	Vacancy
	530.42	73.39	Al_2O_3
1600 °C	531.71	21.05	Aluminosilicate/mullite
	532.45	5.56	Vacancy

Zeiss, Germany). The grain size was counted in terms of the microstructure on the sample cross-section, referring to the ASTM E112–13 standard. TEM thin-section were prepared on FEI Helios G4 UX (Thermo Fischer, USA) using the double-beam focused ion beam-scanning electron microscope (FIB-SEM). TEM/HRTEM analyses were performed using a transmission electron microscope (JEM-2100 F, JEOL Ltd., Tokyo, Japan). The working voltage was 200 kV. The flexural strength of samples was evaluated according to ISO 14704: 2000. The span was 30 mm, and the beam movement speed was 0.5 mm/min. The flexural strength of 7–10 samples was tested for each heat treatment condition, and the results averaged. Microhardness was measured using the Vickers indentation method. The load was 4.903 N, and the holding time was 15 s. The average of ten indentation test results was calculated. The elastic modulus of the samples was evaluated using the rule of mixtures (ROM) with an elastic modulus of 375 GPa [18]. The fracture toughness was calculated according to Eq. (1).

$$\left(\frac{K_{IC}\Phi}{HV\sqrt{d}}\right)\left(\frac{HV}{E_C\Phi}\right)^{0.4} = 0.035\left(\frac{l}{d}\right)^{-1/2} \quad (1)$$

where, K_{IC} was the fracture toughness, HV was the microhardness, E_C was the elastic modulus, Φ was a constraint factor equal to 3, l was the crack length, d was the diagonal size of the indentation. Since $(l + d)/d$ was ≤ 2.5, the crack length referred to the Palmqvist crack length. The average of ten indentation calculations was taken.

3. Results and discussion

3.1. Macro features, thermal, phase, and bonding structure analysis

Fig. 2 shows the macroscopic morphology of the cuboid sample before and after heat treatment and O 1 s element detection results. The sample gradually turns white as the heat treatment temperature

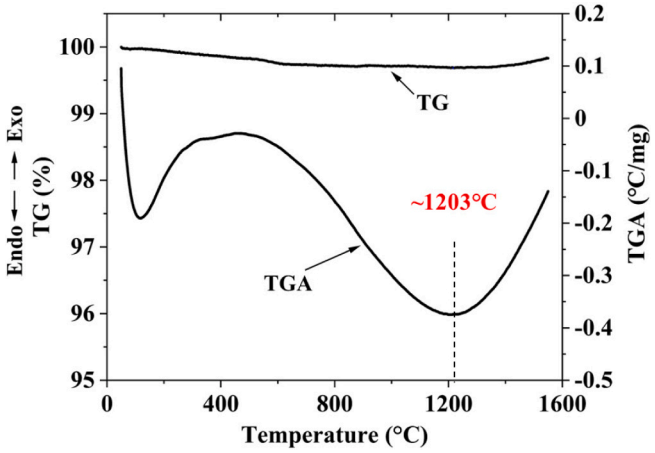

Fig. 3. TG-TGA curves of melt-grown alumina ceramics with trace glass.

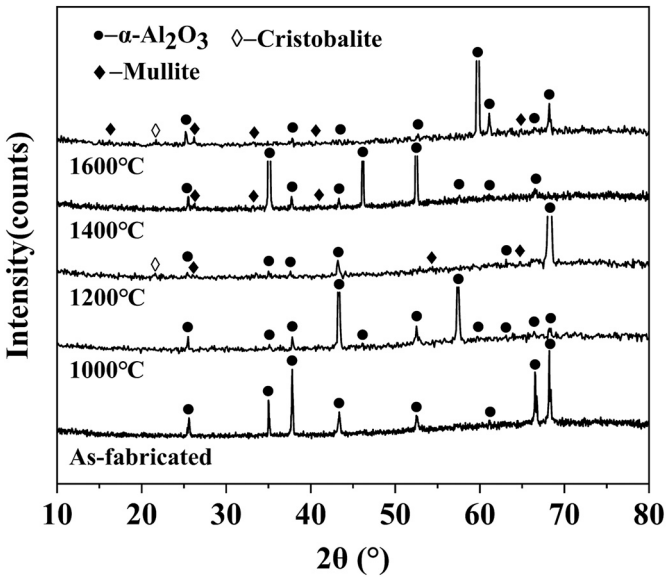

Fig. 4. Phase composition of melt-grown alumina ceramics with trace glass with and without heat treatment.

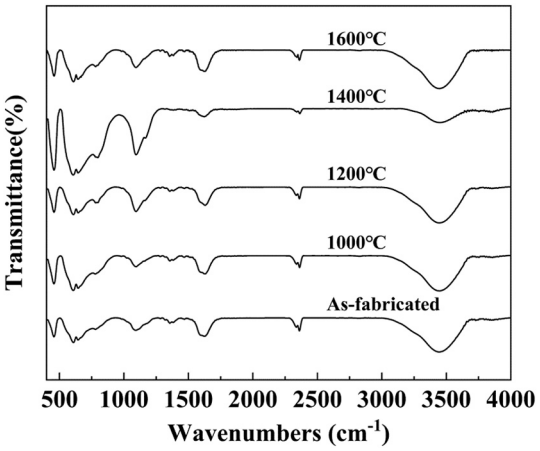

Fig. 5. FT-IR analysis of melt-grown alumina ceramics with trace glass with and without heat treatment.

increases (Fig. 2a). This phenomenon may be attributed to the recovery of oxygen vacancies caused by the laser [8]. Therefore, the XPS technology examined the O 1 s on the sample surface, shown in Fig. 2b. The chemical states of O 1 s on the samples were divided into three types. The peak around 530.5 eV corresponds to Al_2O_3, the peak at 531.7 eV corresponds to aluminosilicate or mullite. The peak around 532.5 eV represents the adsorbed oxygen of the sample. The area percentage of each sub-peak is shown in Table 1. As the heat treatment temperature improved, the concentration of adsorbed oxygen gradually decreased, resulting in the sample color turning gray to white. In addition, it is worth mentioning that the geometry size, e.g., in the length direction, remained essentially unchanged even at temperatures up to 1600 °C (vernier caliper measurements before and after heat treatment were consistent).

Fig. 3 shows the TG/TGA curves of melt-grown alumina ceramics with trace glass fabricated directly by LDED technology heating at 10 °C/min from 50 °C to 1550 °C. On the TG curve, the weight loss was $\leq$ 0.31%. Compared to other oxide fibers (<1.4%) [29], melt-grown alumina ceramics with trace glass have better thermal stability. The endothermic peak at 120 °C represents water. The slight decrease in the sample due to water mass was since the samples were dried at 120 °C for >4 h before DSC was performed. The endothermic peak around 1203 °C may be ascribed to the phase change. Furthermore, XRD was used to detect the phase composition of the melt-grown alumina ceramics with trace glass after heat treatment at different temperatures, shown in Fig. 4. Only the alumina phase in the unheated sample is consistent with the previous report [18]. When the temperature was $\geq$ 1200 °C, cristobalite and mullite formed. The XRD peaks show good agreement with the diffraction peaks of cristobalite [25] and mullite [30] in the reference data. Therefore, the endothermic peak in Fig. 3 at ~1203 °C was "bulging", which may be caused by the formation of cristobalite and mullite.

Fig. 5 shows the results of the bonding structure of the samples with and without heat treatment using Fourier-transform infrared spectroscopy (FT-IR). As shown in Fig. 5, it is difficult to avoid water in the FT-IR samples, even though prepared in a heated state. For example, the IR band at 3444 cm^{-1} was the antisymmetric stretching vibration of -OH, where band intensity was more extensive and more widely distributed, and 1628 cm^{-1} was caused by the bending vibration of H_2O [31]. 2361 cm^{-1} and 2337 cm^{-1} corresponded to the uptake of CO_2 in the air. The vibrational spectra of Al_2O_3 exhibited the longitudinal phonon modes at 1470 cm^{-1}. The antisymmetric stretching vibration of around 1163 cm^{-1} may be a newly formed Al-O-Si structure [32], indicating that the mullitization occurred during the heat treatment. The band of antisymmetric stretching vibration for Si—O in [SiO_4] tetrahedral appeared near 1092 cm^{-1}, which may be caused by SiO_2 and glass crystallization [33]. The bending vibration of Si—O occurred around 457–460 cm^{-1}. The band around 779 cm^{-1} corresponded to the symmetric stretching vibration of [AlO_4] tetrahedral [34].

3.2. Microstructure and grain size

Fig. 6 shows the influence of heat treatment temperature on the microstructure of melt-grown alumina ceramics with trace glass (represented by the cross-section). As shown in Fig. 6, there is no apparent change in the morphology of alumina grains on the cross-section, and the morphology is similar to an equiaxed. The previous study [18] showed that alumina grains were columnar crystals growing along deposition direction, and the microstructure of the sample used in this

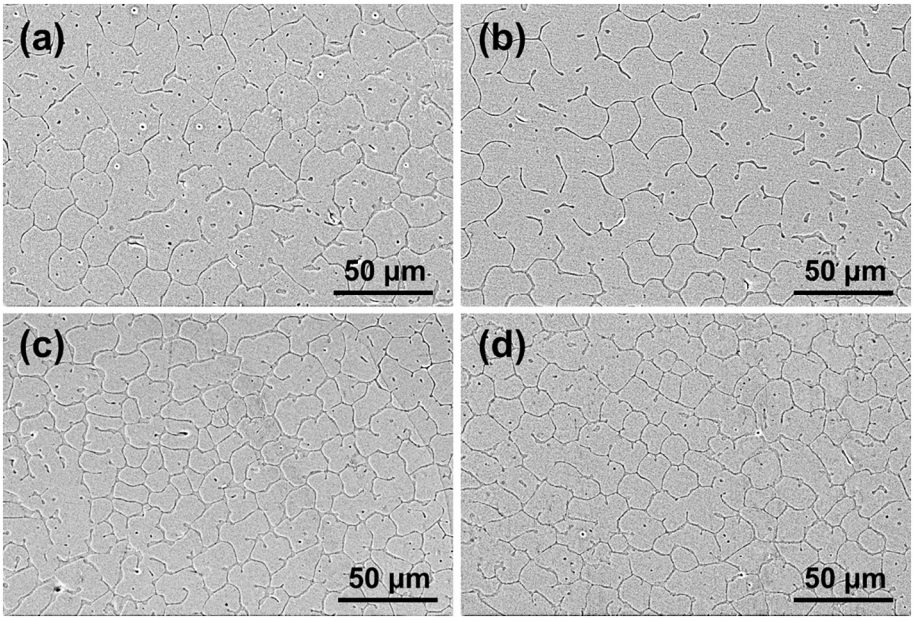

Fig. 6. The influence of heat treatment temperature on the microstructure of melt-grown alumina ceramics with trace glass: (a) 1000 °C; (b) 1200 °C; (c) 1400 °C; (d) 1600 °C.

Table 2
Grain size of melt-grown alumina ceramics with trace glass after heat treatment at different temperatures (in cross-section).

Temperature	As-fabricated	1000 °C	1200 °C	1400 °C	1600 °C
Grain size (μm)	31.06 ± 1.10	29.56 ± 0.63	28.98 ± 0.37	26.57 ± 0.7	25.04 ± 0.73

study is composed of alumina phase and glass phase, in which the glass phase contains elements such as Al, Si, O, etc. The absence of significant changes in grain morphology indicates that the microstructure of melt-grown alumina ceramics with trace glass is stable under high temperatures. However, as the temperature increased, the alumina grain size decreased slightly due to the mullitization reaction at the interface of alumina and glass (Table 2). Fig. 7 shows the high magnification morphology of mullitization. The Si-containing phase distributed between adjacent alumina crystal grains has a contrast difference. The EDS results (Table 3 and Fig. 7) show that point P_1 is alumina, point P_2 is mullite, and point P_3 is Si-rich glass. Thus, mullitization reactions occurred near the alumina-glass interface in the glass. The mullite formation led to a reduction in alumina grain size.

3.3. Phase formation and interface analysis

In order to reveal the formation mechanism of mullite, the samples were analyzed by TEM and HRTEM (Fig. 8 and Fig. 10). Fig. 8 shows typical TEM and HRTEM images of the samples after heat treatment at 1200 °C for 4 h. The following points are noted from Fig. 8. First, the low-magnification morphology shows that the sample consists of alumina (corundum), mullite, and glass (Fig. 8(a)). The SAED patterns confirm alumina and mullite in Fig. 8(c) and Fig. 8(f), respectively. The diffusion of substances in glass melt has the characteristics of short diffusion distance and high diffusion [35]. Idiomorphous mullite has formed from aluminosilicate glass (Fig. 8 (b)). This morphology of mullite is similar to that reported by Wu [36], Adabifiroozjaei [37], Chen [38], and Robert [39]. Mullite crystals grew along the crystallographic [001] direction, confirmed by the SAED pattern (Fig. 8(f)) and high-resolution image (Fig. 8(d)). This growth direction is parallel to laser deposition, resulting from one-dimensional heat dissipation [36] and interface anisotropy of mullite crystals [37]. Adabifiroozjaei suggested that the formation of slow-growing (110) crystal face inhibited the growth of [100] and $[0\bar{1}0]$, believed to grow faster than (001) crystal face, leading to the nucleated mullite developing into the needles. Fig. 8 (d) and Fig. 8(e) show high-resolution images of the mullite-glass interface. The presence of a middle layer with a thickness of about 2 nm is evidence of mullite dissolution in glass and ions (Al^{3+} or Si^{4+}) diffusion at the interface. The crystalline growth of mullite from melt indicates that the growth rate is greater than the dissolution rate into the glass. A similar middle layer existed at the alumina-glass interface, shown in Fig. 8(g, h).

Further, Fig. 9 shows the TEM-EDS results of Fig. 8(a). Point A was alumina with only O and Al elements, without Si elements. In addition to O and Si elements, trace amounts of Al element were detected (point B) in the glass near the alumina-glass interface. Point C was mullite with more Al element than point B. EDS results near the interface prove that alumina dissolved into the glass. This dissolution phenomenon is also discovered in the thermal etching of grain boundaries in traditional refractory materials and glass-containing corundum materials [40]. For example, Guloyan experimentally measured the diffusion of Al^{3+} at 10^{-7}–10^{-8} cm^2/s when corundum refractories dissolved into the glass melt [41]. The diffusion of Al^{3+} into the glass increased the concentration of Al^{3+}, which agrees with Kleebe's research [35]. The reason is that Al^{3+} will break the [SiO_4] tetrahedral structure, reducing melt viscosity. The melt viscosity decreased significantly with increasing Al^{3+} concentration [42], facilitating Al^{3+} diffusion in the glass until the mullite formation. When the concentration of alumina in the glass reaches a value (e.g., saturation), mullite is nucleated and crystallized [43]. The growth of mullite consumed Al in the initial glass, and the Al dissolved in

Table 3
SEM-EDS element point scans of Fig. 7 (at.%).

Position	Al	O	Si	Others
P_1	39.14	60.86	–	–
P_2	33.94	61.15	4.91	–
P_3	21.54	61.07	17.09	0.3

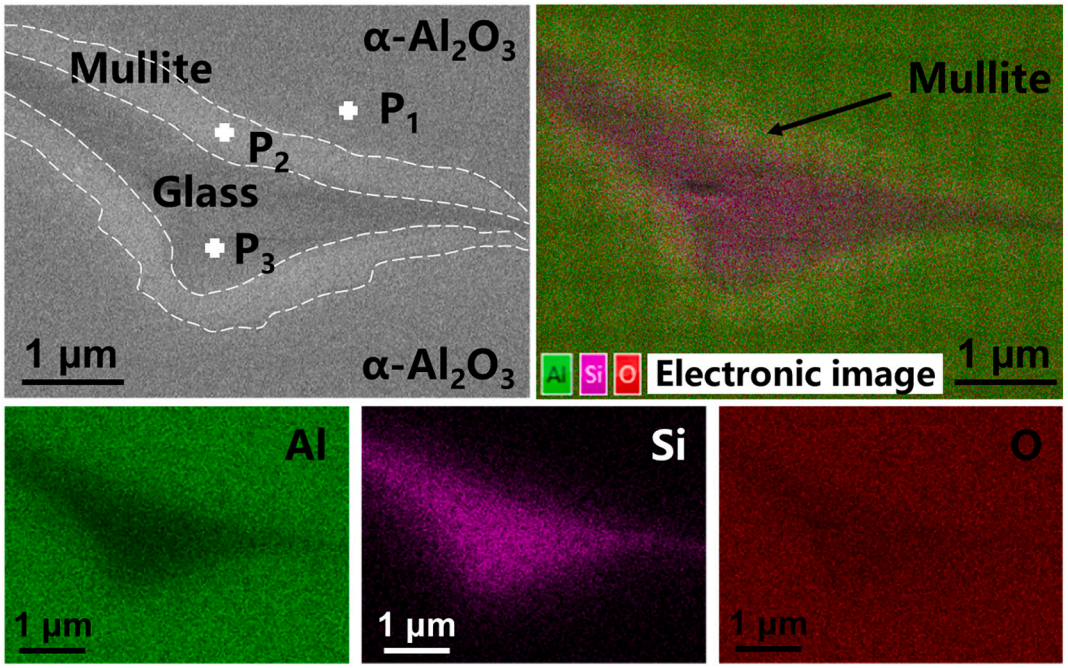

Fig. 7. High-magnification microstructure of mullite formation in melt-grown alumina ceramics with trace glass after heat treatment (1400 °C/4 h).

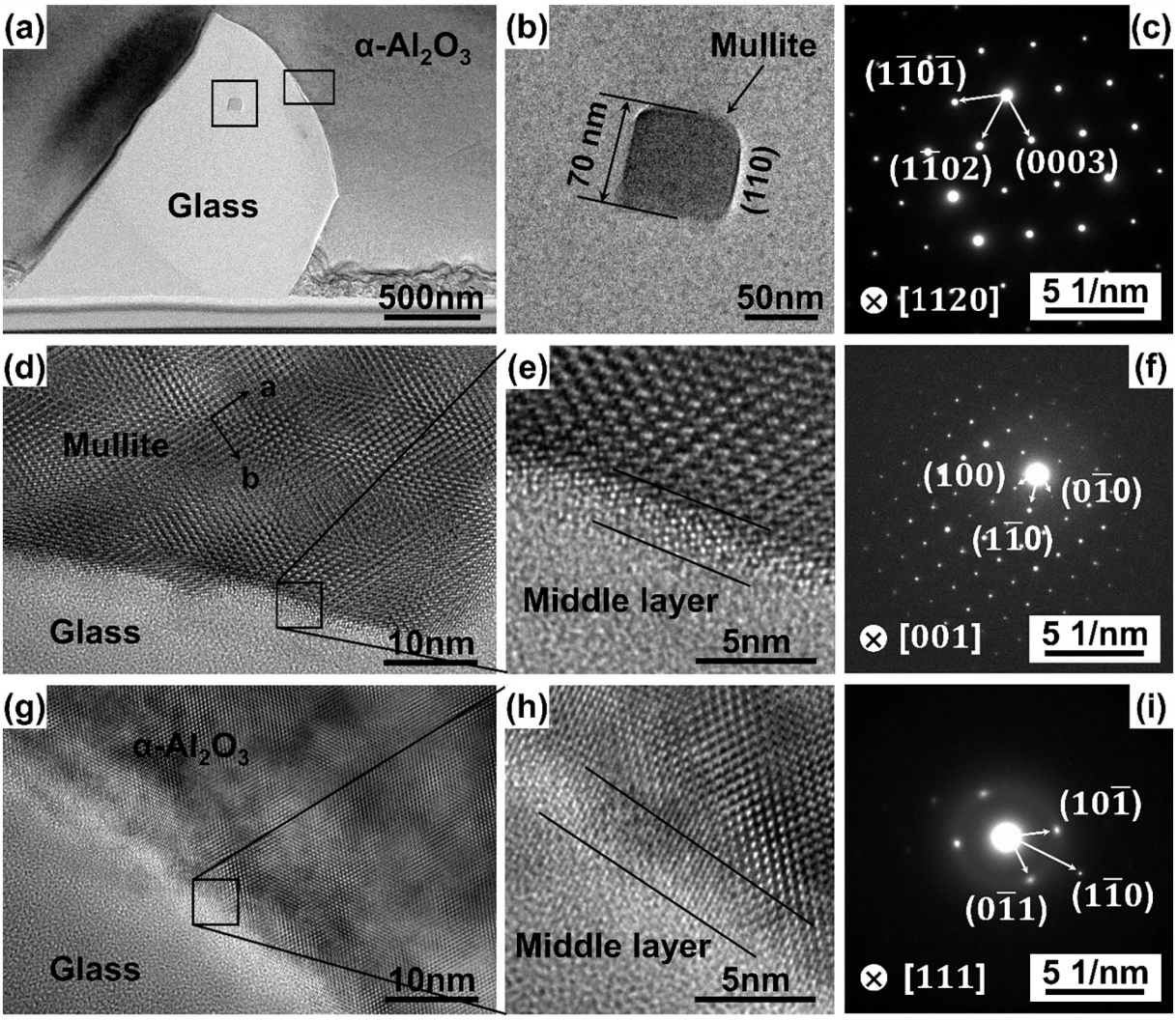

Fig. 8. TEM and HRTEM analysis of melt-grown alumina ceramics with trace glass after heat treatment at 1200 °C for 4 h: (a) TEM morphology, (b) idiomorphous mullite, (c) SAED pattern of α-Al_2O_3, (d) and (e) HRTEM of the mullite-glass interface, (f) SAED pattern of mullite, (g) and (h) was TEM and HRTEM of the α-Al_2O_3-glass interface, (i) SAED pattern of cristobalite.

the glass by corundum, and the final glass phase was Al poor. It can be speculated that amorphous SiO_2 crystallized to form cristobalite (Fig. 4) during the heat treatment. However, no cristobalite was observed from Fig. 8(a). This may be because cristobalite is easily transformed into amorphous SiO_2 due to electron beam sensitivity [44]. The SAED patterns collected directly on a large white phase at low magnification demonstrated that amorphous SiO_2 partially crystallized as cristobalite (Fig. 8(i)). The presence of cristobalite in the Al_2O_3/SiO_2 material system suggests the possibility of mullite formation following the metastable phase diagram. In this work, however, this heat treatment condition (1200 °C/4 h) failed to observe the phase separation of alumina-rich and silica-rich glasses found by MacDowell [45]. It may be related to heat treatment's short holding time (4 h ⟨10*h*) and the presence of impurities (e.g., Na^+). Therefore, the experimental phenomena in Fig. 8 and Fig. 9 show that mullitization reaction occurs near the alumina-glass interface, resulting in a decreasing trend of alumina grain size in the sample.

The TEM observation results of the sample at heat treatment condition of 1600 °C/4 h are shown in Fig. 10, and Fig. 10(a) is the FIB-SEM morphology. In agreement with Fig. 9, the white phase is silica-rich glass, the light phase is mullite, and the dark phase is alumina. The TEM bright-field images clearly show this distribution state (Fig. 10(b)), where Fig. 10(e-1), Fig. 10(f-1), and Fig. 10(f-2) are the SAED patterns of alumina and mullite, and glass phase, respectively. Fig. 10(c) and Fig. 10(d) show the TEM-EDS surface distributions of the Al and Si elements. Under this heat treatment condition, the mullite formed near and far from the alumina/glass interface grows further, attributed to the increase in the diffusion rate. Fig. 10(e) shows the HRTEM morphology at the alumina-glass interface. In the upper part of interface 1, the alumina lattice fringes weaken, which was visual proof of the dissolution of alumina into the glass. The lattice fringe of alumina showed a crystal face spacing $d_{(0003)} = 0.438$ nm (Fig. 10(e-1)). The crystal structure still maintained the trigonal crystal structure of the corundum (Fig. 10(e-2)). Fig. 10(f) shows the HRTEM morphology at the mullite-glass interface (interface 2). The (101) crystal face of mullite formed near interface 2 is tightly bound to the remaining glass. However, the alumina-mullite interface (interface 3) does not appear to be clean, and a middle crystalline layer existed between the two phases (Fig. 10(g)). HRTEM and SAED images show that the middle layer is not composed of single-phase alumina or mullite (Fig. 10(h)). The mullite near interface 3 was formed by the interdiffusion of Al^{3+} and Si^{4+} through this layer. It is noteworthy that the lattice fringe of mullite showed the crystal face spacing $d_{(0\bar{1}1)} = 0.274$ nm. The HRTEM image (Fig. 10(h)) of interface 3 showed that the three phases of alumina, middle layer, and mullite phases were tightly bound.

Based on the above discussion of phase formation and interface

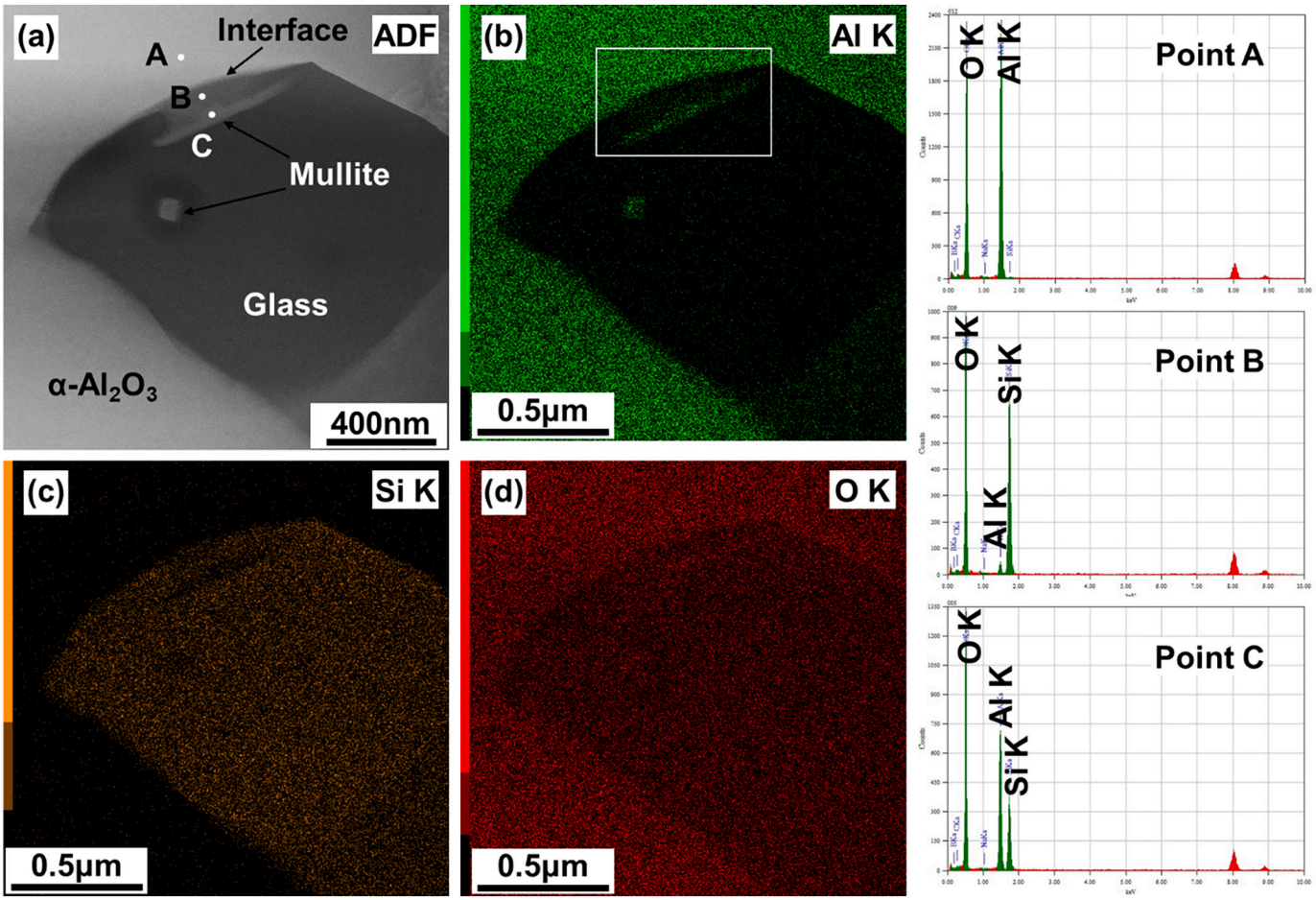

Fig. 9. TEM-EDS analysis of melt-grown alumina ceramics with trace glass after heat treatment at 1200 °C for 4 h.

analysis, the mullitization reaction occurred near the alumina-glass interface in the melt growth alumina with trace glass ceramic under the condition of high-temperature heat treatment. The dissolution of alumina into the glass phase consumes the original alumina grains and reduces the alumina grain size. At low temperature (1200 °C), the mullitization reaction was incomplete (Fig. 8 and Fig. 9(a)), but the alumina grain size decreased slightly (Table 2). With the increase of heat treatment temperature, as shown in Fig. 10, the grain size of mullite reached >5 μm due to the increase of mullite formation content near the interface (Fig. 10(b)). Therefore, the content of alumina consumed increased further and the grain size of alumina decreased further. Finally, the grain size of alumina decreased with the increase of heat treatment temperature.

3.4. Mechanical properties

3.4.1. Flexural strength

Fig. 11 shows the impact of heat treatment temperature on flexural strength. The following points are noted from Fig. 11. First, the flexural strength increased significantly for different temperatures compared to the as-fabricated samples. When the temperature was 1600 °C, the flexural strength reached the highest value of 504.38 ± 28.52 MPa, 62.65% higher than the as-fabricated samples. Second, flexural strength gradually increased with temperature increase, and the increase rate slowed down. Among them, flexural strength at 1000 °C increased by 24.48%. The flexural strength increased from 441.56 ± 24.72 MPa to 482.57 ± 24.8 MPa in the range of 1200 °C to 1400 °C, an increase of 9.29%. In the range of 1400 °C to 1600 °C, the flexural strength growth trend slows down, increasing from 482.57 ± 24.8 MPa to 504.38 ± 28.52 MPa, an increase of 4.5%.

The results in Fig. 11 can be explained by the relaxation of residual stress and crack-healing. First, multi-phase composites prepared by LDED have residual stresses inside, attributed to thermoelastic mismatch formed by the difference in thermal expansion between adjacent phases. Since the shrinkage of alumina ($\alpha_{alumina} = 8 \times 10^{-6}$ K^{-1}) is greater than that of glass ($\alpha_{glass} = 0.55 \times 10^{-6}$ K^{-1}), during the cooling and shrinking of a cylindrical sample, alumina was in tension, and glass was in compression, shown in Fig. 12(a). In addition, there was a possibility of introducing surface residual compressive stresses and microcracks while making cylindrical samples into cuboids using mechanical methods (grinding and polishing). The high-temperature heat treatment of the sample can reduce the stress or even eliminate these defects. Heat treatment performs significantly in metallic materials as an effective method to relieve residual stresses. However, this effect is not always evident for ceramic materials. In this work, no mullite phase formed when the temperature was low (1000 °C). The residual stresses within samples were thoroughly relieved, which was beneficial for strength. After higher temperature (≥ 1200 °C), mullite with low thermal expansion coefficient ($\alpha_{Mullite} = 4.5 \times 10^{-6}$ K^{-1}) formed, which inhibited the release of residual stresses. The reason is that mullite has excellent creep resistance at high temperatures due to diffusion, dislocation, and grain boundary slip [46], which prevents further mitigation of residual stresses, similar to that of SiC nanocomposites reinforced alumina composites [47]. However, the distribution of interphase stress is similar to that in the as-fabricated samples, shown in Fig. 12(b). Chou [48] suggested that the impact of residual stress relaxation only explains a 10% increase in the strength of the composite ceramics. The significant increase of strength in Fig. 11 implies other strengthening mechanisms

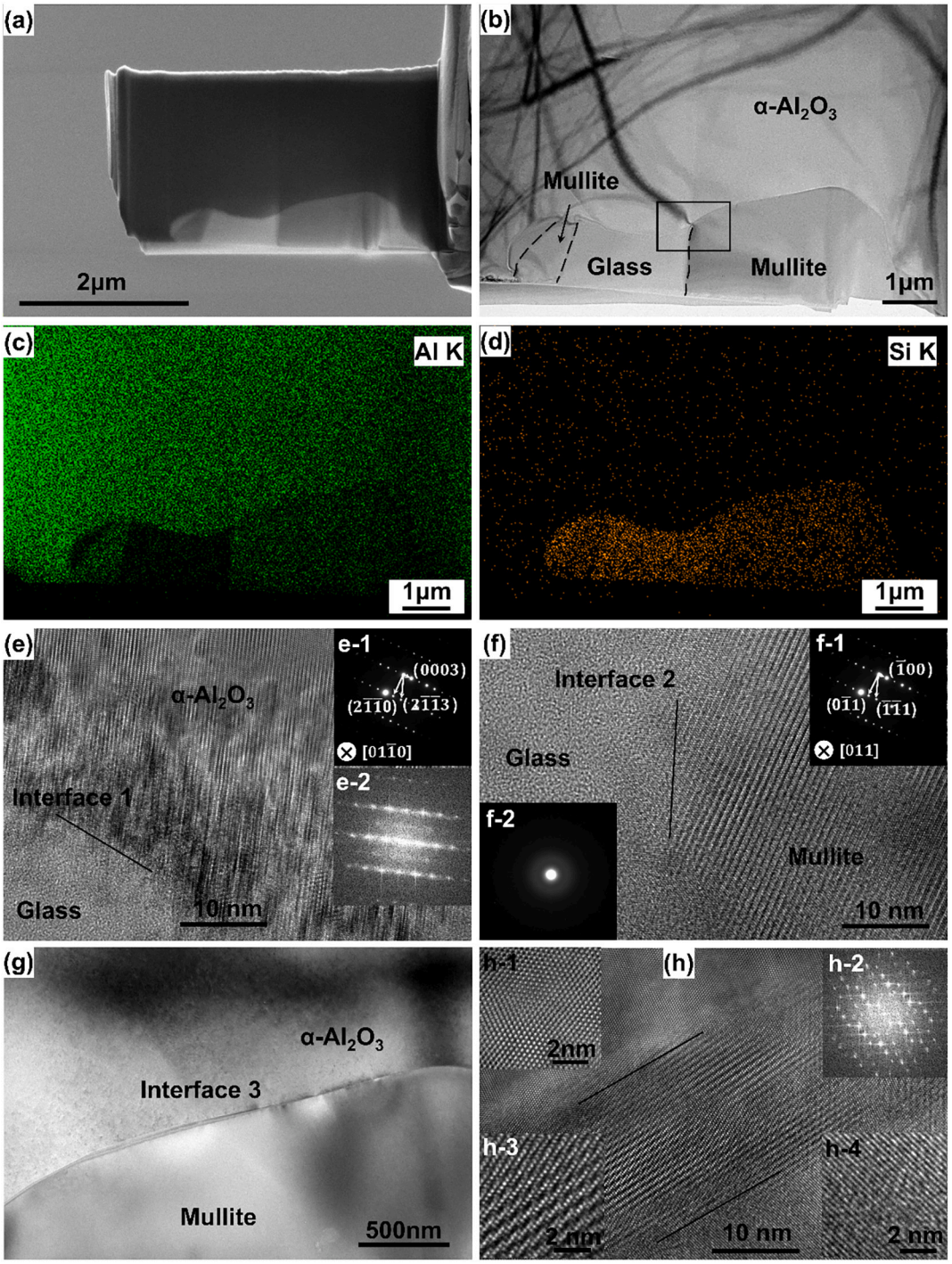

Fig. 10. TEM and HRTEM analysis of melt-grown alumina ceramics with trace glass after heat treatment 1600 °C for 4 h: (a) FIB slice, (b) TEM morphology, (c) Al element, (d) Si element, (e) HRTEM of the α-Al_2O_3-glass interface, (f) HRTEM of the mullite-glass interface, (g) and (h) were TEM and HRTEM of the α-Al_2O_3-glass interface.

besides stress relaxation. The critical flaw size inside the sample was evaluated according to classical strength theory (inset of Fig. 11). The critical flaw size gradually decreased as temperature increased, indicating defect healing occurred during heat treatment. An experiment on the impact of heat treatment on pre-cracks was conducted to verify this judgment. Cracks were induced by the Vickers indentation method, where the load was 1 kgf and the holding time was 30 s. The pre-cracked samples were annealed at different temperatures in an air environment. Fig. 13 shows the crack propagation for unheated and heat treatment at 1400 °C. The alumina surface changed from clean and clear to blurred after heat treatment. The crack fracture surface was significantly blunted, and the adjacent fracture surface had a healing morphology (Fig. 13(b)). The crack surface propagated through alumina grains and deflected or bridged when it met the interface. One should note that no obvious pre-fabricated cracks were observed when the temperature was 1600 °C, which could mean that indentation cracks had healed entirely.

The enhancement of mechanical properties (especially strength) of ceramic materials by crack-healing has been demonstrated by many researchers [22,49–54]. In the present work, at a temperature of 1000 °C, mullite had not yet formed; only alumina and glass existed in

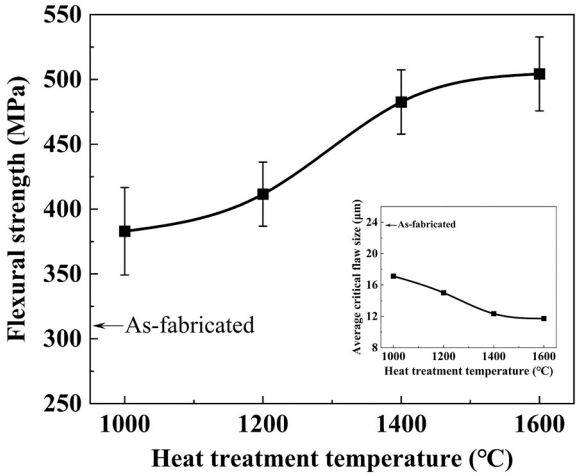

Fig. 11. Influence of heat treatment temperature on the flexural strength of melt-grown alumina ceramics with trace glass.

the sample. Under high-temperature conditions, it is reasonable to assume that liquid glass will undergo viscous flow under the drive of capillary force. As a result, elongated pores or cracks between alumina grains (the small white globules in Fig. 14(a)) healed. This crack-healing mechanism has also been found in alumina/SiC [55]. The reason is that blunting crack tip reduces the stress intensity factor. The EDS results indicated that small white globules were Al-rich glassy with 67.3 wt% aluminas. It is consistent with the TEM analysis of Fig. 8 and Fig. 10. The TEM analysis of Fig. 8 and Fig. 10 illustrates that the white phase is Si-rich, too. When the temperature raised to 1200 °C and the above, glassy liquid phase was squeezed to interface or outside interface due to the mullite formation, developing small white globules (Fig. 14(a) and Fig. 14(c)) or continuous white elongated strips (Fig. 14(c)). It is worth noting that since heat treatment was carried out in an air environment, the water existing at grain surface and crack surface may react with the Si—O bond broken at high temperatures to generate silanol groups, which reduce the viscosity and accelerate the viscous [51]. The bulging morphology of droplets is easily associated with an evaporation-condensation mechanism for crack-healing, and this work did not easily exclude SiO_2 evaporation, which may have a lower boiling point.

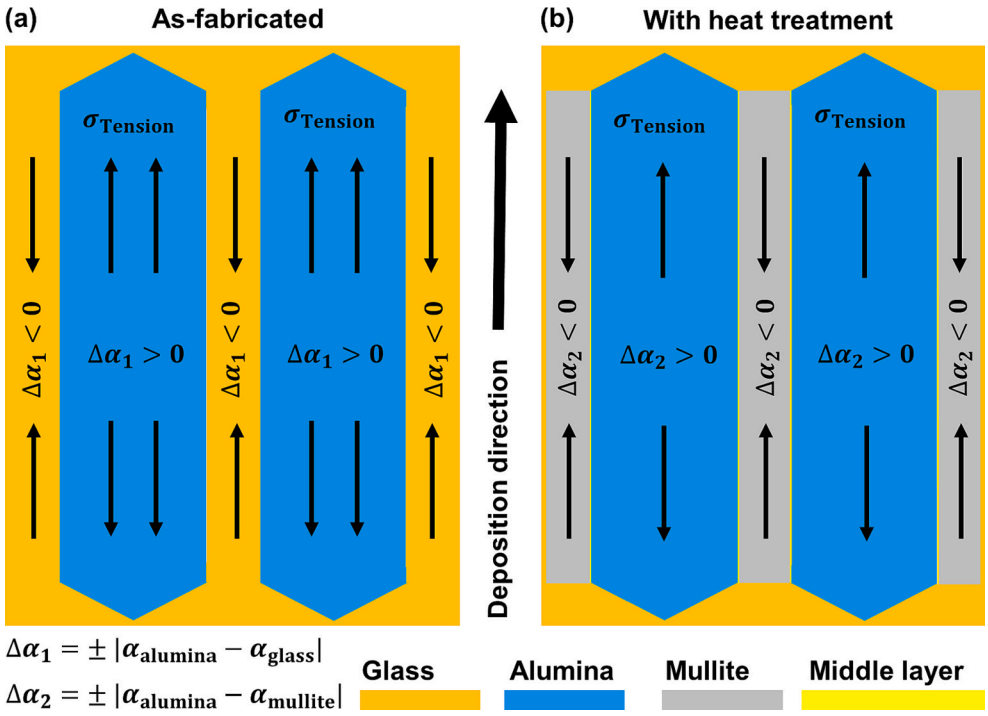

Fig. 12. Schematic diagram of phase structure for melt-grown alumina ceramics with trace glass in the presence of residual stress with arrows. (The size of each phase has been adjusted for ease of presentation).

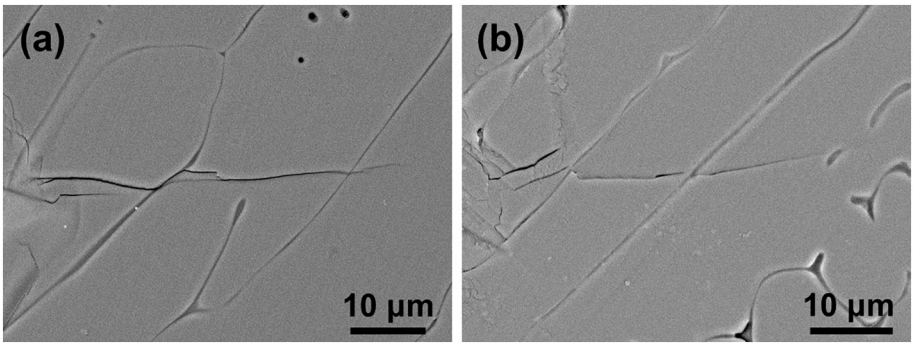

Fig. 13. Low magnification morphology of crack-healing after heat treatment for melt-grown alumina ceramics with trace glass: (a) as-fabricated, (b) 1400 °C/4 h.

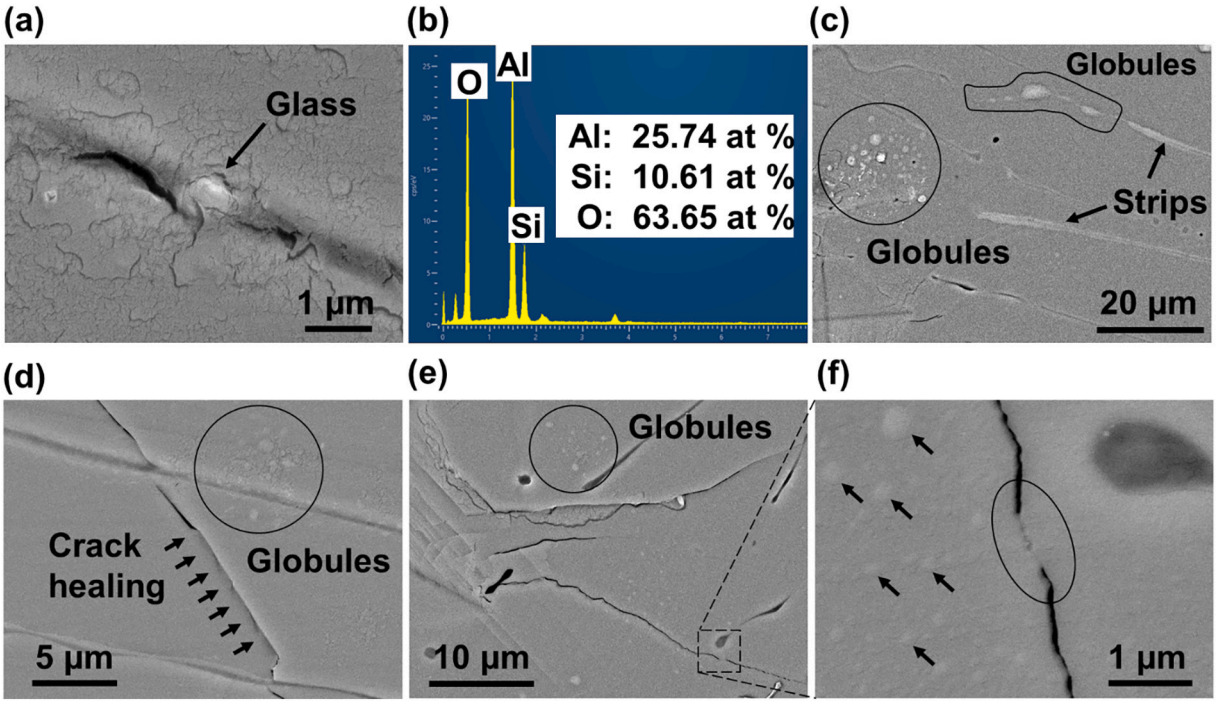

Fig. 14. High magnification morphology and elemental analysis of crack-healing after heat treatment: (a) and (b) 1000 °C; (c) 1200 °C; (d), (e) and (f) for 1400 °C.

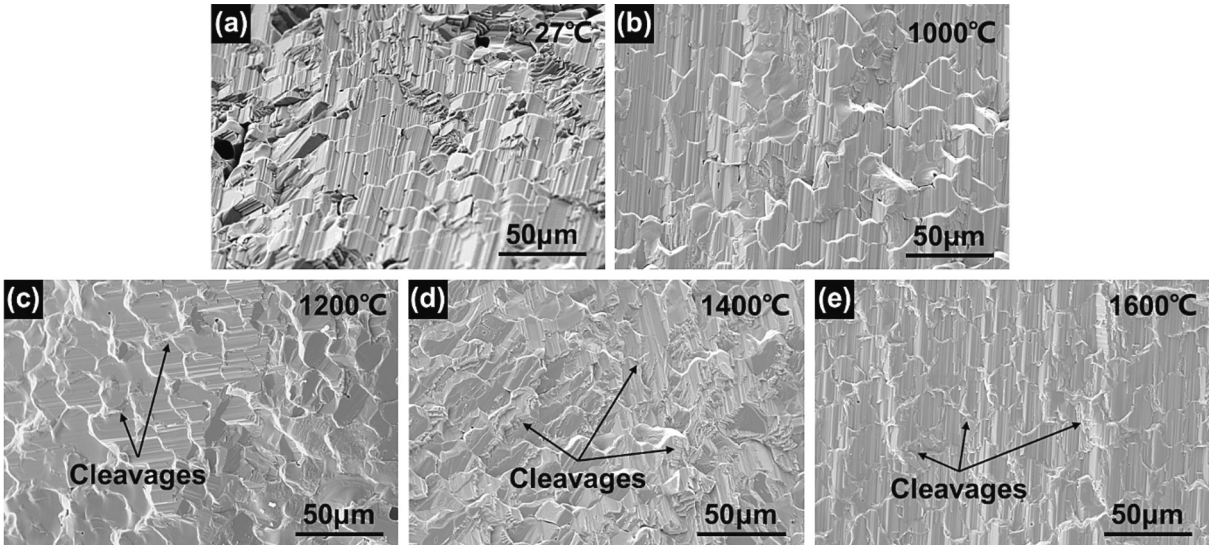

Fig. 15. Bending fracture morphology of melt-grown alumina ceramics with trace glass with and without heat treatment.

Crack-healing inside the alumina grains (Fig. 14(d) and Fig. 14(f)) is caused by diffusion mechanisms and the relaxation of residual indentation stress. The crack-healing rate caused by the diffusion mechanism is expressed as [56]:

$$\frac{\partial a}{\partial t} = \frac{C}{T} exp\left(-\frac{Q}{kT}\right) \tag{2}$$

where, $\partial a/\partial t$ is the crack-healing rate, T is the temperature, Q is the diffusion activation energy, and k is the Boltzmann's constant.

$$C = \frac{\pi D_0 \gamma \Omega}{R^2 k ln(L_0/R)} \tag{3}$$

where, D_0 is the diffusion coefficient, γ is the surface free energy, Ω is the atomic volume, R is the curvature radius of the crack tip, and L_0 is the distance from crack edge to external body surface. Obviously, the rate of crack-healing increases with the increase of temperature, so heat treatment is beneficial to the crack-healing of materials. The flattening of strength increases at a temperature of 1600 °C may be due to the increase in mullite content impedes the crack-healing driven by the viscous flow of glass. Therefore, based on the above analysis, it is believed that there are many possible mechanisms leading to crack-healing, and the role proportion of various mechanisms needs to be further characterized and analyzed.

The fracture morphology of three-point bending further illustrates the influence of heat treatment temperature on strength, shown in Fig. 15. After heat treatment, fracture morphology gradually evolved from clean and clear cleavage planes to a fuzzy shape, consistent with the results illustrated in Fig. 13. This feature indicates that crack-healing

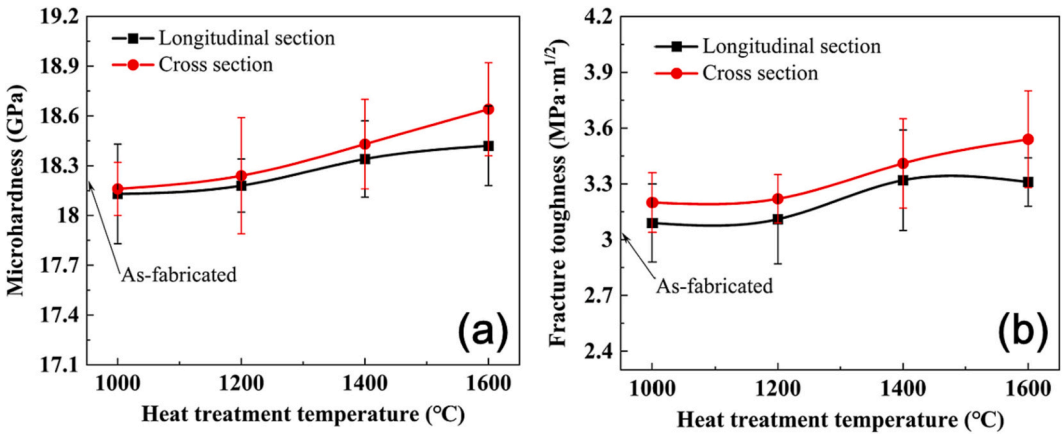

Fig. 16. Influence of heat treatment on microhardness (a) and fracture toughness (b) of melt-grown alumina ceramics with trace glass.

occurred during the heat treatment. At low temperature (1000 °C), the sample maintained a mixed fracture mechanism with an intergranular and transgranular fracture on alumina grains, which is similar to the sample without heat treatment (Fig. 15(a)). At a medium temperature (e.g., 1200 °C), bending fracture is influenced by the tightly bound interface (alumina-middle layer-mullite, shown in Fig. 15(a)) and crack-healing. In addition to transgranular fracture within alumina grains, small-scale cleavages representing transgranular fracture were formed between alumina grains near the interface (Fig. 15(c)). The small-scale cleavages were visible in the bending fractures at higher temperatures (1400 °C and 1600 °C), shown in Fig. 15(d) and Fig. 15(e). Therefore, the formation of small-scale cleavages at the interface further explained the influence of heat treatment temperature on strength.

3.4.2. Microhardness and fracture toughness

The temperature as a function of surface microhardness and fracture toughness of the samples is shown in Fig. 16. The microhardness at the temperature of 1000 °C was comparable to that of as-fabricated samples. The microhardness slowly increased with temperature (Fig. 16(a)). The maximum value reached 18.64 GPa at 1600 °C, increasing 2.47% compared to as-fabricated samples. The slight increase in microhardness is attributed to the reduction in alumina grain size. The fracture toughness showed a similar pattern, that is, increased with increasing temperature, with a maximum value of 3.54 MPa·$m^{1/2}$, an increase of 16.83% compared to the as-fabricated. The increase in fracture toughness was attributed to heat treatment [14]. Specifically, under the condition of high-temperature heat treatment, the occurrence of crack-healing will lead to the passivation of crack tip inside material and reduce local stress at the tip [57,58], which is a possible reason for improving the fracture toughness of the material. In addition, the formation of mullite strongly combined with alumina leads to the formation of small-scale cleavages when the material breaks, as shown in Fig. 15, which shows that the energy required for crack tip growth is increased, easy to form crack bridging and other toughening mechanisms [18], and increases the ability to resist crack growth.

4. Conclusion

This work investigated a heat treatment method that significantly improved the performance (especially strength) of the melt-grown alumina ceramics with trace glass prepared by LDED. The results provide an effective route for preparing high-performance melt-grown alumina-based ceramics by LDED, which has significant applications in the rapid fabrication of high-performance advanced ceramics for hot-end components. The main conclusions are:

1) The decrease in adsorbed oxygen concentration with increasing temperature is responsible for the gradual whitening of the sample. The melt-grown alumina ceramics with trace glass fabricated by LDED technology are thermally stable in the range of 50–1550 °C, and the sample weight decreased by 0.31%. The sample undergoes a phase change during the heat treatment. Without heat treatment, the samples have only corundum and glass phases. When the temperature is 1200 °C and above, mullite formed from the glass melt, and the glass partially crystallized into cristobalite.
2) After heat treatment, the grain morphology of alumina remained essentially unchanged, indicating that mullite formation did not significantly affect the morphology of alumina. However, the alumina grain size was slightly reduced to a small extent, attributed to the dissolution of alumina into the glass and the formation of mullite near the alumina-glass interface. When the temperature was≥ 1200 °C, a middle layer formed between alumina and glass, and Al^{3+} and Si^{4+} diffused through the middle layer under high temperature to increase mullite content. The mullite formation position is in the glass near the alumina-glass interface and the glass away from the interface. After high-temperature heat treatment (e.g., 1600 °C), the interface bond between alumina, the newly formed middle layer, and mullite were tight.
3) The mechanical properties of melt-grown alumina ceramics with trace glass had been significantly improved after heat treatment. Specifically, flexural strength first increased and then decreased, with a maximum increase of 62.65%. Crack-healing occurred in melt-grown alumina ceramics with trace glass during heat treatment. The strength increase was attributed to residual stress relief and crack-healing. Possible crack-healing mechanisms are the viscous flow of glass, evaporation-condensation, and diffusion. Fracture toughness gradually increased, with a maximum increase of 16.83%. Crack-healing leading to passivation of defects (such as cracks) in the samples explained the increased fracture toughness.

Declaration of Competing Interest

The authors declare that they have no known competing financial interests or personal relationships that could have appeared to influence the work reported in this paper.

Data availability

Data will be made available on request.

Acknowledgements

Supported by the National Natural Science Foundation of China (No.

51805070, No. 51790172), the Natural Science Foundation of Liaoning Province (No. 2019-ZD-0010, No.2020-BS-057), and the Fundamental Research Funds for the Central Universities (No. DUT19RC(3)060). The authors thank the Shenzhen Science and Technology Innovation Commission for the financial support numbered as JSGG20210420091802007.

References

[1] T. Froeliger, A. Després, L. Toualbi, D. Locq, M. Veron, G. Martin, R. Dendievel, Interplay between solidification microsegregation and complex precipitation in a γ/γ' cobalt-based superalloy elaborated by directed energy deposition, Mater. Charact. 194 (2022), 112376, https://doi.org/10.1016/j.matchar.2022.112376.

[2] T.J. Pirzada, D. Liu, J. Ell, H. Barnard, I. Šulák, M. Galano, T.J. Marrow, R. O. Ritchie, In situ observation of the deformation and fracture of an alumina-alumina ceramic-matrix composite at elevated temperature using x-ray computed tomography, J. Eur. Ceram. Soc. 41 (2021) 4217–4230, https://doi.org/10.1016/j.jeurceramsoc.2021.01.030.

[3] C. Fellah, J. Braun, C. Sauder, F. Sirotti, M.H. Berger, Influence of the carbon interface on the mechanical behavior of SiC/SiC composites, Compos. Pt. A-Appl. Sci. Manuf. 133 (2020) 105867, https://doi.org/10.1016/j.compositesa.2020.105867.

[4] F. Christin, Design, fabrication, and application of thermostructural composites (TSC) like C/C, C/SiC, and SiC/SiC composites, Adv. Eng. Mater. 4 (2002) 903–912, https://doi.org/10.1002/adem.200290001.

[5] J.L. Lei, Q.R. Zhang, Y.H. Wang, H.B. Zhang, Direct laser melting of Al_2O_3 ceramic paste for application in ceramic additive manufacturing, Ceram. Int. 48 (2022) 14273–14280, https://doi.org/10.1016/j.ceramint.2022.01.315.

[6] D. Wu, X. Yu, Z. Zhao, G. Ma, C. Zhou, B. Zhang, G. Ren, F. Niu, One-step additive manufacturing of TiCp reinforced Al_2O_3–ZrO_2 eutectic ceramics composites by laser directed energy deposition, Ceram. Int. (2022), https://doi.org/10.1016/j.ceramint.2022.12.141. In Press.

[7] Y. Waku, N. Nakagawa, T. Wakamoto, H. Ohtsubo, K. Shimizu, Y. Kohtoku, A ductile ceramic eutectic composite with high strength at 1,873 K, Nature 389 (1997) 49–52, https://doi.org/10.1038/37937.

[8] H. Liu, H. Su, Z. Shen, D. Zhao, Y. Liu, Y. Guo, M. Guo, J. Zhang, L. Liu, H. Fu, Preparation of large-size Al_2O_3/$GdAlO_3$/ZrO_2 ternary eutectic ceramic rod by laser directed energy deposition and its microstructure homogenization mechanism, J. Mater. Sci. Technol. 85 (2021) 218–223, https://doi.org/10.1016/j.jmst.2021.01.025.

[9] Y.Z. Li, Y.B. Hu, W.L. Cong, L. Zhi, Z.N. Guo, Additive manufacturing of alumina using laser engineered net shaping: effects of deposition variables, Ceram. Int. 43 (2017) 7768–7775, https://doi.org/10.1016/j.ceramint.2017.03.085.

[10] M. Dezaki, A. Serjouei, A. Zolfagharian, M. Fotouhi, M. Moradi, M.K.A. Ariffin, M. Bodaghi, Experimental investigation on laser directed energy deposition based additive manufacturing of Al_2O_3 bulk structures, Ceram. Int. 47 (2021) 5708–5720, https://doi.org/10.1016/j.ceramint.2020.10.157.

[11] Y. Lakhdar, C. Tuck, J. Binner, A. Terry, R. Goodridge, Additive manufacturing of advanced ceramic materials, Prog. Mater. Sci. 116 (2021), 100736, https://doi.org/10.1016/j.pmatsci.2020.100736.

[12] S.A. Rasaki, D. Xiong, S. Xiong, F. Su, M. Idrees, Z. Chen, Photopolymerization-based additive manufacturing of ceramics: a systematic review, J. Adv. Ceram. 10 (2021) 442–471, https://doi.org/10.1007/s40145-021-0468-z.

[13] C. Wei, Z. Zhang, D. Cheng, Z. Sun, M. Zhu, L. Li, An overview of laser-based multiple metallic material additive manufacturing: from macro- to micro-scales, Int. J. Extreme Manuf. 3 (2020), 012003, https://doi.org/10.1088/2631-7990/abce04.

[14] V.K. Balla, S. Bose, A. Bandyopadhyay, Processing of bulk alumina ceramics using laser engineered net shaping, Int. J. Appl. Ceram. Tec. 5 (2008) 234–242, https://doi.org/10.1111/j.1744-7402.2008.02202.x.

[15] F. Niu, D. Wu, F. Lu, G. Liu, G. Ma, Z. Jia, Microstructure and macro properties of Al_2O_3 ceramics prepared by laser engineered net shaping, Ceram. Int. 44 (2018) 14303–14310, https://doi.org/10.1016/j.ceramint.2018.05.036.

[16] Y. Huang, D. Wu, D. Zhao, F. Niu, G. Ma, Investigation of melt-growth alumina/aluminum titanate composite ceramics prepared by directed energy deposition, Int. J. Extreme Manuf. 3 (2021), 035101, https://doi.org/10.1088/2631-7990/abf71a.

[17] S. Yan, Y.F. Huang, D.K. Zhao, F.Y. Niu, G.Y. Ma, D.J. Wu, 3D printing of nano-scale Al_2O_3-ZrO_2 eutectic ceramic: principle analysis and process optimization of pores, Addit. Manuf. 28 (2019) 120–126, https://doi.org/10.1016/j.addma.2019.04.024.

[18] D. Zhao, D. Wu, J. Shi, F. Niu, G. Ma, Microstructure and mechanical properties of melt-grown alumina-mullite/glass composites fabricated by directed laser deposition, J. Adv. Ceram. 11 (2021) 1–9, https://doi.org/10.1007/s40145-021-0518-6.

[19] Y. Liu, C. Wang, T. Liu, Effect of annealing on quality enhancement of micro-machining green alumina ceramics by laser ablation, Ceram. Int. 47 (2021) 30273–30286, https://doi.org/10.1016/j.ceramint.2021.07.207.

[20] W. Zheng, J.-M. Wu, S. Chen, C.-S. Wang, C.-L. Liu, S.-B. Hua, K.-B. Yu, J. Zhang, J.-X. Zhang, Y.-S. Shi, Influence of Al_2O_3 content on mechanical properties of silica-based ceramic cores prepared by stereolithography, J. Adv. Ceram. 10 (2021) 1381–1388, https://doi.org/10.1007/s40145-021-0513-y.

[21] R. He, N. Zhou, K. Zhang, X. Zhang, L. Zhang, W. Wang, D. Fang, Progress and challenges towards additive manufacturing of SiC ceramic, J. Adv. Ceram. 10 (2021) 637–674, https://doi.org/10.1007/s40145-021-0484-z.

[22] F. Tavangarian, D. Hui, G. Li, Crack-healing in ceramics, Compos. B Eng. 144 (2018) 56–87, https://doi.org/10.1016/j.compositesb.2018.02.025.

[23] K. Shahzad, J. Deckers, J.-P. Kruth, J. Vleugels, Additive manufacturing of alumina parts by indirect selective laser sintering and post processing, J. Mater. Process. Tech. 213 (2013) 1484–1494, https://doi.org/10.1016/j.jmatprotec.2013.03.014.

[24] J.G. Heinrich, A. Gahler, J. Gunster, M. Schmücker, J. Zhang, D. Jiang, M. Ruan, Microstructural evolution during direct laser sintering in the Al_2O_3-SiO_2 system, J. Mater. Sci. 42 (2007) 5307–5311, https://doi.org/10.1007/s10853-006-1247-5.

[25] D. Gailevičius, V. Padolskytė, L. Mikoliūnaitė, S. Šakirzanovas, S. Juodkazis, M. Malinauskas, Additive-manufacturing of 3D glass-ceramics down to nanoscale resolution, Nanoscale Horiz. 4 (2019) 647–651, https://doi.org/10.1039/c8nh00293b.

[26] Z. Fan, Y. Zhao, M. Lu, H. Huang, Yttria stabilized zirconia (YSZ) thin wall structures fabricated using laser engineered net shaping (LENS), Int. J. Adv. Manuf. Technol. 105 (2019) 4491–4498, https://doi.org/10.1007/s00170-019-03322-z.

[27] H. Liu, H. Su, Z. Shen, D. Zhao, Y. Liu, Y. Guo, J. Zhang, L. Liu, H. Fu, Insights into high thermal stability of laser additively manufactured Al_2O_3/$GdAlO_3$/ZrO_2 eutectic ceramics under high temperatures, Addit. Manuf. 48 (2021), 102425, https://doi.org/10.1016/j.addma.2021.102425.

[28] M. Schmucker, F. Flucht, H. Schneider, High temperature behaviour of polycrystalline aluminosilicate fibres with mullite bulk composition. I. Microstructure and strength properties, J. Eur. Ceram. Soc. 16 (1996) 281–285, https://doi.org/10.1016/0955-2219(95)00152-2.

[29] R. Jiang, H. Liu, L. Yang, X. Sun, H. Cheng, Mechanical properties of aluminosilicate fiber heat-treated from 800 °C to 1400 °C: effects of phase transition, grain growth and defects, Mater. Charact. 138 (2018) 120–126, https://doi.org/10.1016/j.matchar.2018.01.047.

[30] L. Reinders, S. Pfeifer, S. Kröner, H. Stolpmann, A. Renfftlen, L.C. Greiler, B. Clauß, M.R. Buchmeiser, Development of mullite fibers and novel zirconia-toughened mullite fibers for high temperature applications, J. Eur. Ceram. Soc. 41 (2021) 3570–3580, https://doi.org/10.1016/j.jeurceramsoc.2020.12.048.

[31] L.F. Zhang, W. Xia, X. Liu, W.Q. Zhang, Synthesis of titanium cross-linked chitosan composite for efficient adsorption and detoxification of hexavalent chromium from water, J. Mater. Chem. A 3 (2015) 331–340, https://doi.org/10.1039/c4ta05194g.

[32] C.H. Rüscher, Phonon spectra of 2:1 mullite in infrared and Raman experiments, Phys. Chem. Miner. 23 (1996) 50–55, https://doi.org/10.1007/BF00202993.

[33] S. Shoval, B. Champagnon, G. Panczer, The quartz-cristobalite transformation in heated chert rock composed of micro and crypto-quartz by micro-Raman and FT-IR spectroscopy methods, J. Therm. Anal. Calorim. 50 (1997) 203–213, https://doi.org/10.1007/bf01979562.

[34] P. Tarte, Infra-red spectra of inorganic aluminates and characteristic vibrational frequencies of AlO_4 tetrahedra and AlO_6 octahedra, Spectrochim. Acta Mol. Spectros. 23 (1967) 2127–2143, https://doi.org/10.1016/0584-8539(67)80100-4.

[35] H.J. Kleebe, F. Siegelin, T. Straubinger, G. Ziegler, Conversion of Al_2O_3-SiO_2 powder mixtures to 3:2 mullite following the stable or metastable phase diagram, J. Eur. Ceram. Soc. 21 (2001) 2521–2533, https://doi.org/10.1016/S0955-2219(01)00275-8.

[36] D. Wu, D. Zhao, Y. Huang, F. Niu, G. Ma, Shaping quality, microstructure, and mechanical properties of melt-grown mullite ceramics by directed laser deposition, J. Alloy Compd. 871 (2021), 159609, https://doi.org/10.1016/j.jallcom.2021.159609.

[37] E. Adabifiroozjaei, J.N. Hart, P. Koshy, D.R.G. Mitchell, C.C. Sorrell, Mullite-glass and mullite-mullite interfaces: analysis by molecular dynamics (MD) simulation and high-resolution TEM, J. Am. Ceram. Soc. 101 (2018) 428–439, https://doi.org/10.1111/jace.15169.

[38] Y.-F. Chen, M.-C. Wang, M.-H. Hon, Secondary mullite formation in kaolin-Al_2O_3 ceramics, J. Mater. Res. 19 (2004) 806–814, https://doi.org/10.1557/jmr.2004.19.3.806.

[39] R.F. Davis, J.A. Pask, Diffusion and reaction studies in the system Al_2O_3-SiO_2, J. Am. Ceram. Soc. 55 (1972) 525–531, https://doi.org/10.1111/j.1151-2916.1972.tb13421.x.

[40] S.C. Whipkey, M.C. Modugno, H. Lee, W.M. Carty, Optimized etching of porcelain and polycrystalline alumina with a glass phase, J. Eur. Ceram. Soc. 41 (2021) 3761–3768, https://doi.org/10.1016/j.jeurceramsoc.2021.01.035.

[41] Y.A. Guloyan, O.M. Pustyl'Nikov, Diffusion kinetics in the reaction of corundum refractories with a glass melt, Glas. Ceram. 63 (2006) 346–350, https://doi.org/10.1007/s10717-006-0119-4.

[42] G. Wu, E. Yazhenskikh, K. Hack, E. Wosch, M. Müller, Viscosity model for oxide melts relevant to fuel slags. Part 1: pure oxides and binary systems in the system SiO_2–Al_2O_3–CaO–MgO–Na_2O–K_2O, Fuel Process. Technol. 137 (2015) 93–103, https://doi.org/10.1016/j.fuproc.2015.03.025.

[43] M. Schmucker, W. Albers, H. Schneider, Mullite formation by reaction sintering of quartz and α-Al_2O_3 - a TEM study, J. Eur. Ceram. Soc. 14 (1994) 511–515, https://doi.org/10.1016/0955-2219(94)90121-X.

[44] A. Cernok, K. Marquardt, R. Caracas, E. Bykova, G. Habler, H.-P. Liermann, M. Hanfland, M. Mezouar, E. Bobocioiu, L. Dubrovinsky, Compressional pathways of α-cristobalite, structure of cristobalite X-I, and towards the understanding of seifertite formation, Nat. Commun. 8 (2017) 1–10, https://doi.org/10.1038/ncomms15647.

[45] J.F. MacDowell, G.H. Beall, Immiscibility and crystallization in Al_2O_3-SiO_2 glasses, J. Am. Ceram. Soc. 52 (1969) 17–25, https://doi.org/10.1111/j.1151-2916.1969.tb12653.x.

[46] S. Komarneni, in: H. Schneider (Ed.), Mullite, John Wiley & Sons, Weinheim, 2006.

[47] J. Fang, H.M. Chan, M.P. Harmer, Residual stress relaxation behavior in Al_2O_3-SiC nanocomposite, Mat. Sci. Eng. A-struct. 195 (1995) 163–167, https://doi.org/10.1016/0921-5093(94)06515-2.
[48] I.A. Chou, H.M. Chan, M.P. Harmer, Effect of annealing environment on the crack healing and mechanical behavior of silicon carbide-reinforced alumina nanocomposites, J. Am. Ceram. Soc. 81 (1998) 1203–1208, https://doi.org/10.1111/j.1151-2916.1998.tb02469.x.
[49] P. Greil, Generic principles of crack-healing ceramics, J. Adv. Ceram. 1 (2013) 249–267, https://doi.org/10.1007/s40145-012-0020-2.
[50] T. Osada, K. Kamoda, M. Mitome, T. Hara, T. Abe, Y. Tamagawa, W. Nakao, T. Ohmura, A novel design approach for self-crack-healing structural ceramics with 3D networks of healing activator, Sci. Rep. 7 (2017) 17853, https://doi.org/10.1038/s41598-017-17942-6.
[51] C. Wang, H. Wang, R. Gao, M. Zhang, S.W. Liu, J. Hou, X. Chen, Experimental investigation on thermal healing of subsurface damage in borosilicate glass, Ceram. Int. 47 (2021) 17128–17138, https://doi.org/10.1016/j.ceramint.2021.03.022.
[52] X. Lu, S. Li, W. Zhang, B. Yao, W. Yu, Y. Zhou, Crack healing behavior of a MAB phase: MoAlB, J. Eur. Ceram. Soc. 39 (2019) 4023–4028, https://doi.org/10.1016/j.jeurceramsoc.2019.05.059.
[53] S. Li, G. Song, K. Kwakernaak, S. van der Zwaag, W.G. Sloof, Multiple crack healing of a Ti_2AlC ceramic, J. Eur. Ceram. Soc. 32 (2012) 1813–1820, https://doi.org/10.1016/j.jeurceramsoc.2012.01.017.
[54] S. Li, L. Xiao, G. Song, et al., Oxidation and crack healing behavior of a fine-grained Cr_2AlC ceramic, J. Am. Ceram. Soc. 96 (2013) 892–899, https://doi.org/10.1111/jace.12170.
[55] P. Rajak, R.K. Kalia, A. Nakano, P. Vashishta, Faceting, grain growth, and crack healing in alumina, ACS Nano 12 (2018) 9005–9010, https://doi.org/10.1021/acsnano.8b02484.
[56] R.N. Stevens, R. Dutton, The propagation of Griffith cracks at high temperatures by mass transport processes, Mat. Sci. Eng. A-struct. 8 (1971) 220–234, https://doi.org/10.1016/0025-5416(71)90076-0.
[57] R.O. Ritchie, The conflicts between strength and toughness, Nature Mater. 10 (2011) 817–822, https://doi.org/10.1038/nmat3115.
[58] S.R. Choi, V. Tikare, Crack healing of alumina with a residual glassy phase: strength, fracture toughness and fatigue, Mat. Sci. Eng. A-struct. 171 (1993) 77–83, https://doi.org/10.1016/0921-5093(93)90394-T.